Influence of reduced Na vacancy concentrations in the sodium superionic conductors $Na_{11+x}Sn_2P_{1-x}M_xS_{12}$ (M = Sn, Ge)

Marvin A. Kraft[a], Lara M. Gronych[a], Theodosios Famprikis[b], Wolfgang G. Zeier*[a,c]

[a]*Institute of Inorganic and Analytical Chemistry, University of Muenster, Corrensstrasse 28/30, D-48149 Muenster, Germany.*

[b]*Department of Radiation Science and Technology Delft, University of Technology, Mekelweg 15, Delft 2629JB, The Netherlands*

[c]*Helmholtz Institut Muenster, FZ Jülich, Corrensstrasse 46, D-48149 Münster, Germany.*

Abstract

Exploration of sulfidic sodium solid electrolytes and their design contributes to advances in solid state sodium batteries. Such design is guided by a better understanding of fast sodium transport, for instance in the herein studied $Na_{11}Sn_2PS_{12}$-type materials. By using Rietveld refinements against synchrotron X-ray diffraction and electrochemical impedance spectroscopy, the influence of aliovalent substitution onto the structure and transport in $Na_{11+x}Sn_2P_{1-x}M_xS_{12}$ with M = Ge and Sn is investigated. Whereas Sn induces stronger structural changes than Ge, the found influence on the sodium sublattice and the ionic transport properties are comparable. Overall, a reduced in-grain activation energy of Na^+ transport can be found with the reducing Na^+ vacancy concentration. This work explores previously unreported phases in the $Na_{11}Sn_2PS_{12}$ structure type that, based on their determined properties reveal Na^+ vacancy concentrations to be an important factor guiding further understanding within $Na_{11}Sn_2PS_{12}$-type materials.

1. Introduction

Along with lithium solid-state batteries, that promise high energy density by usage of lithium metal anodes,[1] sodium based solid-state batteries may be a prospectively cheaper energy storage option.[2] Solid electrolytes represent a key enabler of the technology as optimizing their ionic transport, electrochemical stability and processability can improve overall cell performance significantly.[1,3,4] Therefore, the understanding of ionic transport and its relation to the structural features present in solid electrolytes has been widely investigated in Li^+- and Na^+-conducting structural families such as LISICONs[5], NASICONs[6–8], $(Li/Na)_3MCl_6$ halides[9–11], (*closo*-) borohydrates[12–14], but also prominently in the sulfide-based material classes: argyrodites[15–18] and ternary thio-LISICONs[19,20]. Other promising compounds are the Na_3PS_4-type[21] as well as the $Li_{10}GeP_2S_{12}$-type[22] conductors, all of which have been reviewed in depth elsewhere.[23] Derived from $Li_{10}GeP_2S_{12}$, the Na^+ equivalent $Na_{11}Sn_2PS_{12}$ (NaSnPS) crystallizes in a distinct but related structure type, which has shown promising ionic transport properties. In addition, this class shows the ability of being structurally tunable by isovalent substitutions of P with Sb and S with Se, as well as aliovalent substitution of P with Si or Sn with Sb.[24–29]

The $Na_{11}Sn_2PS_{12}$ structure (Figure 1) is comprised of SnS_4 and PS_4 tetrahedral units building up the anionic backbone that is filled with Na^+ ions in the tetragonal $I4_1/acd$ space group with $Z = 8$ formula units per unit cell. The large unit cell (quadrupling that of $Li_{10}GeP_2S_{12}$) originates from the long-range rotational ordering (90° rotation along the *c* direction [001]) of the PS_4^{3-} tetrahedra (P(1) on an 8*a* Wyckoff site) located in half of the "body-centered" positions of a simple cubic arrangement of SnS_4^{4-} units (Sn(1) 16*e* Wyckoff site). Those SnS_4^{4-} tetrahedra also show rotational ordering leading to faces of SnS_4^{4-} tetrahedra that are oriented towards the PS_4^{3-} tetrahedra. The vertices of the SnS_4^{4-} tetrahedra point towards the other half of "body-centered" sites forming a quasi-cubic void (Na(6)). This arrangement leads to a distortion of SnS_4 tetrahedra along the *a*- and *b*- ([100] and [010]) directions from ideal "simple-cubic" ordering. As this distortion follows the PS_4^{3-} rotation and tetrahedral size it can be captured by a linear relation of relative rotational angles between PS_4^{3-} units and the lattice parameter ratio *c/a*, expressing isotropic expansion upon atomic substitution.[25] Within this anionic backbone 7 distinct sites are relevant for the sodium sub-lattice description. In $Na_{11}Sn_2PS_{12}$ five sodium sites are found highly occupied: Na(1) a Wyckoff 32*g* site and Na(2) a Wyckoff 16*d* site, residing in Na(*X*)S_6 polyhedra that are sharing an edge with the PS_4^{3-} units. Both sites usually show lower Na occupation than the other three

octahedrally coordinated sites: the Na(3) on a 16*e* site, Na(4) on a 16*c* site and Na(5) on a 16*f* site. Especially on the Na(4) and Na(5) sites, large thermal displacement ellipsoids were reported and a splitting of the Na(4) site has been used to describe the Na^+ distribution in that octahedron.[25,27] Furthermore, the quasi-cubic 8*b* site hosts the Na(6), which bridges the Na(1) and Na(2) positions and was shown to take part in the diffusion mechanism by molecular dynamics simulations.[24,30–33] Lastly, another unoccupied 32*g* site in an octahedral void has been discussed as the intermediate site in alternative diffusion pathways on the basis of bond valence sum analyses.[27,28] The sodium distribution over those sites seems to be heavily influenced by substitutions as, for example, the Na(6) site occupancy (at 298 K) in $Na_{11.1}Sn_{2.1}P_{0.9}Se_{12}$ was reported to be 74% while the site remains lowly occupied (< 22%) in $Na_{11}Sn_2PS_{12}$.[23,24,27,28]

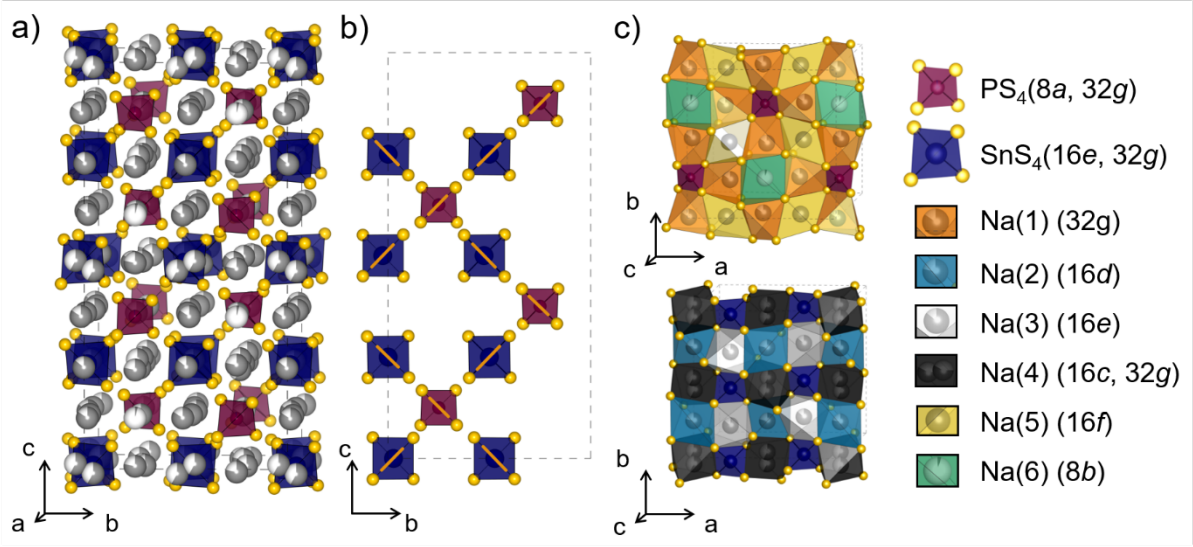

Figure 1: a) Crystal structure of $Na_{11}Sn_2PS_{12}$, showing the Na^+ channels within the polyanionic backbone of SnS_4^{4-} and PS_4^{3-} tetrahedra. b) By depicting only half of those tetrahedra (Sn in front of P; Sn in x = 0.75, P in x = 0.5) in the unit cell in the bc plane and highlighting the tetrahedral edges oriented towards the a-direction, the rotational ordering in b and c plane is presented. SnS_4^{4-} tetrahedra are rotated with respect to each other ~90° along all three spatial dimensions leading to their faces oriented towards the PS_4^{3-} tetrahedra, which itself are rotated ~90° with respect to each other in the c direction. c) The resulting Na-S polyhedra in this polyanionic backbone are shown in the two respective slabs of PS_4^{3-} (z = 0.125) and SnS_4^{4-} (z = 0) along the c-direction.

To improve the transport properties through substitution, the ratio of immobile cations in the framework is often discussed as the phase width of the $Na_{11}Sn_2PS_{12}$-type structure may be quite narrow in the relevant quasi-binary or even quasi-ternary phase diagrams.[25,27] For instance, in the first two publications isolating the $Na_{11}Sn_2PS_{12}$ structure in the series of

$Na_{10+d}Sn_{1+d}P_{2-d}S_{12}$ between $0 \leq d \leq 1$, a strict phase segregation into $Na_{11}Sn_2PS_{12}$ and Na_3PS_4 was found.[24,27] Additionally, in the $Na_{12-h}Sn_{3-h}Sb_hS_{12}$ series the phase width was explored, showing that altering the Na concentration within the $Na_{11}Sn_2PS_{12}$-type phase seems to influence the ionic conductivity minimally.[29] However, in another aliovalent substitution approach controlling the Na^+ content and thereby the charge carrier concentration *via* phosphorus exchange, i.e. in $Na_{12-j}[Sn_2Si]_{1-j}P_jS_{12}$, reduced activation energies and a drastic improvement of ionic conductivities was observed.[34] Moreover, the ratio between Sn and Sb in $Na_{11+x}Sn_{2+x}(Sb_{1-y}P_y)_{1-x}S_{12}$ was altered[25] to form full solid solutions thereby basically performing an aliovalent substitution in respect to $Na_{11}Sn_2SbS_{12}$.[29] This highlighted the importance of the cationic ratio for phase stability, however, the influence of a stoichiometric excess of sodium has been entirely neglected. Additionally, theoretical investigations predict likely synthesizable phases of $Na_{9+s}Sn_sPn_{3-s}S_{12}$ with *Pn* = P, Sb within $1.5 < s < 2.5$,[31] but no changes to ionic conductivity or activation energy were found in $Na_{11\pm o}Sn_2PS_{12}$ with altering the Na concentration by one sodium ion per unit cell ($o = 0.125$).[32]

Inspired by the question of how strongly vacancies may affect the ionic transport in this class of materials, in this work we synthesized and characterized the series of $Na_{11+x}Sn_2P_{1-x}M_xS_{12}$ with *M* = Ge and Sn. Systematically altering the Na^+ (and with it the vacancy-) concentration shows influences on the ionic transport within these materials. Full structural characterization by Rietveld refinements against synchrotron X-ray diffraction data reveals the expansion of the unit cell *via* substitution within the $(P_{1-\delta}M_\delta)S_4$ and $(Sn_{1-\varepsilon}M_\varepsilon)S_4$ tetrahedral units. Alongside the reduced Na^+-vacancy concentration (with lattice expansion) a reduction of in-grain activation energy for ionic transport is found. As previously observed in the $Na_{11}Sn_2PS_{12}$ structural family, the reduced activation energy leads to an overall reduced room temperature in-grain sodium ionic conductivity.[25,28,35] This work further highlights how aliovalent substitution and changing Na^+ carrier densities influence the ionic transport properties in this class of materials.

2. Experimental Methods

Synthesis. All samples in the series $Na_{11+x}Sn_2P_{1-x}M_xS_{12}$ with *M* = Ge, Sn were prepared by solid-state synthesis. Therefore, the starting materials Na_2S (Merck, 99.98%), SnS_2 (Kojundo, 99.9+%), P_2S_5 (Merck, 99%), GeS (Merck, 99.99%) and S (Acros Organics, 99.999 %) were mixed in the respective stoichiometric ratios for 15 minutes in an agate mortar. The resulting precursor mixtures were pressed into pellets, which were subsequently transferred into a

dried (2 h at 800 °C under dynamic vacuum p < 2 mbar) quartz ampoule. The reaction was carried out at 650 °C for 12 h with a heating rate of 40 °C/h and a cooling rate of 60 °C/h in a tube furnace. The obtained yellowish product pellets were ground to a powder in an agate mortar for further characterization purposes. All powders were handled under exclusion of air and moisture by handling under inert (argon) atmosphere or vacuum.

Synchrotron X-ray powder diffraction. High resolution synchrotron X-ray powder diffraction was carried out at the 11-BM-B beamline of the Advanced Photon Source at the Argonne National Laboratory. All samples were sealed into glass capillaries and placed inside the Kapton® tubes mounted onto sample holders. The diffraction experiment was carried out at a wavelength of 0.457894 Å over a 2θ range of 0.5° to 50° with a step width of 0.001° and at a temperature of 100 K to "freeze out" the mobile sodium ions.

Rietveld analysis. Rietveld refinements were carried out using the TOPAS-Academic V6 software.[36] Fit indicators: R_{wp}, R_{exp}, and goodness of fit (*gof)* were used to assess the quality of the refined structural models. The (1) background was fit by a Chebychev polynomial with 15 parameters, a (2) zero error was refined from the starting value provided by the beamline. The Bragg reflection shape was fit by the (3) Thompson-Cox-Hastings modified pseudo-Voigt function implemented in TOPAS and corrected for (4) asymmetry with a simple axial divergence model. For structural parameters of the main $Na_{11}Sn_2PS_{12}$ type phase (in space group $I4_1/acd$, origin setting 2) the tetragonal (5) lattice parameters a and c, subsequently the (6) fractional coordinates, (7) thermal displacement parameters and (8) site occupancy factors (*sof*) of the respective sites were refined. Identified side phases were taken into account in the refinements to reduce the impact of overlapping reflections. Therefore, the structural information reported in the literature was retained and the reflection shape, intensity and lattice parameters were allowed to refine. To finalize a refinement all parameters mentioned above were allowed to vary collectively.

Concerning the structural parameters refined, certain constraints had to be employed to lead to physically reasonable values (*e.g.* atomic distances, charge balancing). All constraints applied are tabulated in the Supporting Information (Table S1 and S8). In structures within $Na_{11+x}Sn_2P_{1-x}Sn_xS_{12}$ the distribution of tin and phosphorous was allowed over both, the Sn(1) (16*c*) and P(1) (8*a*), immobile cation sites. Within $Na_{11+x}Sn_2P_{1-x}Ge_xS_{12}$ the additional cation limits the resolvable atomic contrast over the Sn(1) and P(1) sites. Based on the low content of phosphorous on the Sn(1) site within structures of $Na_{11+x}Sn_2P_{1-x}Sn_xS_{12}$, in accordance with

literature,[24,26,27] only Ge and Sn were distributed over the Sn(1) (16*c*) site. Hence, P, Ge and Sn are distributed over the P(1) (8*a*) site with the Sn content fixed to 2, while refining the Ge content in the structures. Similar to previous work, the sodium sub-lattice in all structures was constrained to equal isotropic thermal displacement parameters (B_{eq}) and the total sodium content was constrained for charge balance following the refined phosphorous content in the structures.[25] As previously reported, the original 16*e* Wyckoff Na(4) site was split into a 32*g* Wyckoff site.[25] To be consistent within the whole series this split Na(4) site (32*g*) was also introduced in samples with $x_M > 0.5$ in $Na_{11+x}Sn_2P_{1-x}M_xS_{12}$ (M = Ge, Sn) even though the distance of adjacent Na(4) sites reduced below 1 Å. In those cases the *sof* on the split Na(4) site was limited to a maximum of 0.5. All structural data are tabulated in Tables S2 – S13.

Bond valence site energies. The bond valence site energies for mobile Na^+ within $Na_{11}Sn_2PS_{12}$ were calculated starting from the refined structure using the softBV-GUI software.[37] The standard grid resolution of 0.1 Å and the automatically estimated screening factor of 0.627344 was used for the energy landscape calculation.[37] The crystal structure and surfaces of equivalent bond valence site energy were visualized with the VESTA[38] software, to map the connectivity of Na sites within the sodium sublattice.

Electrochemical impedance spectroscopy. Electrical conductivities were measured by AC impedance spectroscopy. Therefore, the powders were isostatically pressed at 325 MPa for 45 minutes. The obtained pellets were sintered for 10 minutes at 550 °C under vacuum in dried quartz ampoules. The ~ 90% dense pellets (pellet dimensions included in the Supporting Information Table S14 and S15) were contacted with 200 nm thick Au electrodes (0.82 cm diameter) via thermal evaporation and aluminum contacts in a pouch cell configuration.[39] Low temperature impedance spectra from −100 °C to 25 °C (Novocool Cryosystem) were collected with a Novocontrol Alpha-A frequency analyzer (Novocontrol Technologies, Montabaur, Germany) applying a sinusoidal voltage curve of V_{rms} = 50 mV amplitude, necessary to resolve high resistances in the frequency range from 10 MHz to 100 mHz. The obtained spectra were evaluated utilizing the RelaxIS 3 - Impedance Spectrum Analysis software (rhd instruments, Darmstadt, Germany).

3. Results and Discussion

Structural characterization. To determine the influence of increasing the Na^+ content in this materials class, two series of solid solutions, $Na_{11+x}Sn_2P_{1-x}M_xS_{12}$ with $M = Ge$, Sn and $0 \leq x_M \leq 0.625$, are synthesized. The structural parameters are determined by Rietveld refinement against synchrotron X-ray data at 100 K. Low temperature diffraction data was used to make sure all Na^+ positions can be reliably refined in this fast ionic conductor and previous work shows a good comparison between low- and room-temperature data.[25] Comparison between the series of the aliovalent substituents Ge and Sn highlights the similarities between the systems in which the cation substituents exhibit different sizes, while overall similar stoichiometric Na^+ contents are present in the respective compositions. Exemplary Rietveld refinements are shown in Figure 2. The other diffraction patterns and the corresponding refinements can be found in the Supporting Information (Figure S1 & S2).

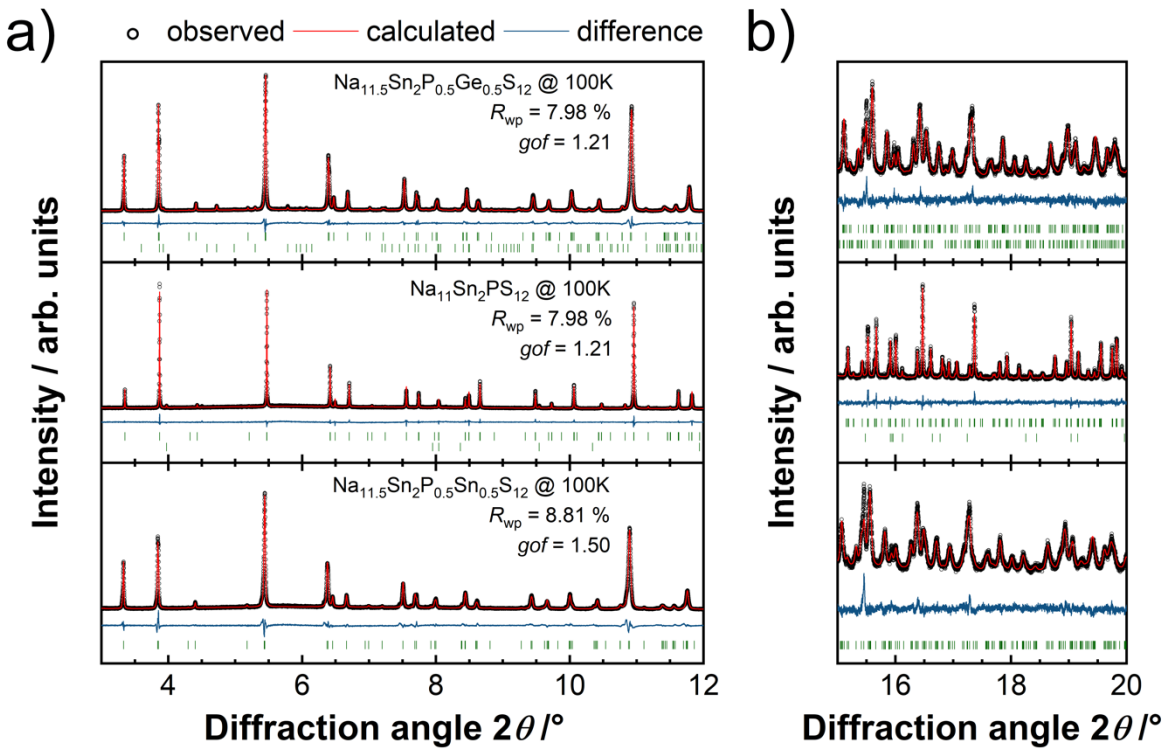

Figure 2: a) Representative Rietveld refinements against the synchrotron X-ray diffraction patterns (λ = 0.457894 Å) of $Na_{11.5}Sn_2P_{0.5}Ge_{0.5}S_{12}$, $Na_{11}Sn_2PS_{12}$ and $Na_{11.5}Sn_2P_{0.5}Sn_{0.5}S_{12}$ at 100 K. Collected data is presented as black data points, the calculated pattern and respective difference curves from refinement are shown as red and blue lines. The obtained reflection positions of the main phases are depicted as green tick marks. Small amounts (1.2 wt %) of $NaSnS_2$ and (2.9 wt %) of $Na_6Sn_2S_7$ type side-phase can be observed in $Na_{11}Sn_2PS_{12}$ and $Na_{11.5}Sn_2P_{0.5}Ge_{0.5}S_{12}$ with corresponding reflection

positions indicated by the respectively lower green tick marks. b) Zoom-in on higher diffraction angles to show the quality of the fit.

Figure 3a shows the total refined fraction of Ge and Sn in the compositions, denoted as $x_{M,\mathrm{ref}}$. A linear increase is found initially that corresponds to a full solubility, however, deviations from linearity are found at higher Ge and Sn fractions suggesting that a solubility limit has been reached. For instance, in $Na_{11.625}Sn_2P_{0.375}Sn_{0.625}S_{12}$ ~8 wt % of Na_4SnS_4 side-phase indicate the solubility limit to lie in the range of $0.5 < x_{Sn} \leq 0.625$, which is in line with the refined total Sn composition in Figure 3a. In the case of $Na_{11.625}Sn_2P_{0.375}Ge_{0.625}S_{12}$ the situation appears more complex. Besides the main phase, small amounts of a different $Na_{11}Sn_2PS_{12}$ phase are revealed by the synchrotron X-ray diffraction that exert themselves as additional reflections and shoulders shifted to lower 2θ angles (Figure S3), indicating some *M* enriched phase. These are only resolved in synchrotron diffraction data and indicate a miscibility gap and accordingly at $x_{Ge} = 0.625$ a deviation from linearity is found. This observation highlights the complexity of the phase diagram, especially when introducing an additional atom type into a quaternary compound. Similar effects have been reported for P-introduction in $Na_{12}Sn_2SiS_{12}$.[34] Furthermore, it shows the possibility of closely related phases coexisting that are most likely thermodynamically stabilized by significant entropic contribution from the possible rearrangement of Na atoms as well as immobile cation disorder.[31,40]

The lattice parameters *a* and *c* (Figure 3b) within $Na_{11+x}Sn_2P_{1-x}Sn_xS_{12}$ as well as the resulting unit cell volume (Figure 3c) show a linear increase up to $Na_{11.625}Sn_2P_{0.375}Sn_{0.625}S_{12}$, despite the limited solubility. Such linearity indicates the successful substitution of P^{5+} ($r^i_{CN4}(P^{5+}) = 0.17$ pm), with the smaller Shannon ionic radius, by Sn^{4+} ($r^i_{CN4}(Sn^{4+}) = 0.60$ pm).[41] In $Na_{11+x}Sn_2P_{1-x}Ge_xS_{12}$ the expansion of the lattice with x_{Ge} is not as pronounced as in $Na_{11+x}Sn_2P_{1-x}Sn_xS_{12}$ with the difference in ionic radius between P^{5+} and Ge^{4+} not as large as when substituting with Sn^{4+} ($r^i_{CN4}(P^{5+}) = 0.17$ pm < $r^i_{CN4}(Ge^{4+}) = 0.39$ pm < $r^i_{CN4}(Sn^{4+}) = 0.60$ pm)[41]. Considering the overall minute changes (1.2% of unit cell volume), a mostly linear expansion behavior of the lattice parameters *a* and *c* (see Figure 3b) as well as the resulting unit cell volume is found up to $x_{Ge} \leq 0.625$.

The isotropy of the expansion, expressed in the ratio of lattice parameters *c*/*a* (Figure S3), in the $Na_{11}Sn_2PS_{12}$ structure type has been previously shown to be linearly correlated with the rotational angles between respective $(P_{1-\delta}M_\delta)S_4$ tetrahedra.[25] This correlation equally holds in

the compounds reported here (Figure S3b). The increase of the lattice parameters *a* and *c* as well as the overall expansion of the unit cell volume (Figure 3c) is driven mainly by the expansion of the $(P_{1-\delta}M_\delta)S_4$ tetrahedra upon introduction of the tetrel substituents. The linear expansion of $(P_{1-\delta}Sn_\delta)S_4$ tetrahedral volumes with x_{Sn} further confirms the successful substitution of phosphorous with tin in $Na_{11+x}Sn_2P_{1-x}Sn_xS_{12}$. Despite the mixed occupancy of P/Ge/Sn on the P(1) site in the $Na_{11+x}Sn_2P_{1-x}Ge_xS_{12}$ series (Figure S3c), the expansion of the $(P_{1-\delta}M_\delta)S_4$ tetrahedra proceeds approximately linearly with nominal x_{Ge}.

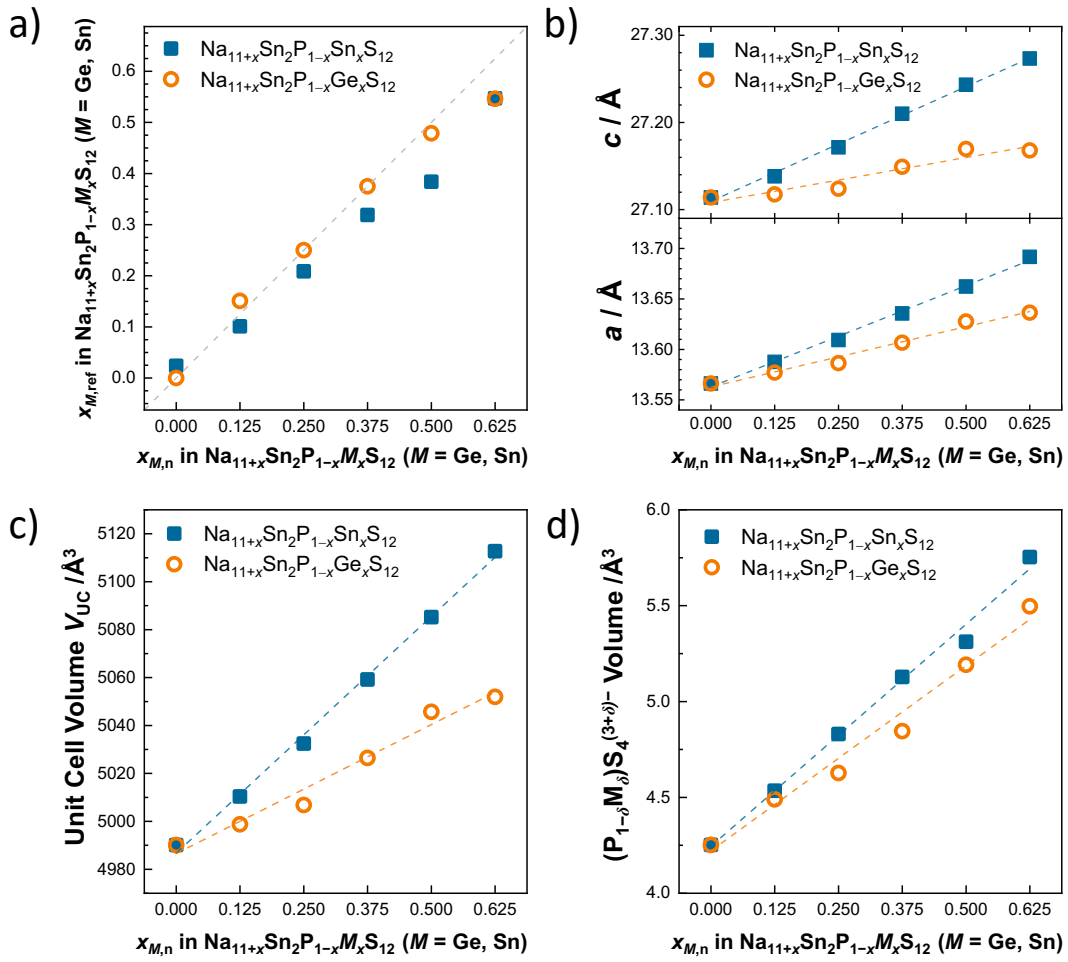

Figure 3: a) Nominal x_n vs. refined x_{ref} contents of M = Ge, Sn in $Na_{11+x}Sn_2P_{1-x}M_xS_{12}$. With increasing nominal content x_n, a lattice expansion is observed in the tetragonal lattice parameters b) a and c as well as in the resulting c) unit cell volume of the $Na_{11+x}Sn_2P_{1-x}M_xS_{12}$ M = Ge, Sn series. d) Locally, Sn and Ge substitute mainly on the P(1) site where the expansion of the $(P_{1-\delta}M_\delta)S_4$ tetrahedra (as the global average determined by the powder X-ray diffraction) is representative of the successful replacement of P. Refinement uncertainties are smaller than or comparable in size to data points and linear fits act as guides to the eye.

Sodium ion sublattice.

Within the series of solid solutions M = Ge, Sn in $Na_{11+x}Sn_2P_{1-x}M_xS_{12}$, the changing polyanionic framework as well as the altered Na^+ concentration are expected to influence the sodium sublattice. Expressed as the occupancies on the six distinct Na sites and the coordination polyhedra around them, the Na^+ substructure is extracted from the structural models refined against low-temperature synchrotron X-ray diffraction. Whereas previous studies investigated the complex $Na(X)S_n$ polyhedral connectivity, it has shown useful to separate the six Na-S polyhedra present into two locally connected clusters as highlighted by bond valance maps depicted in Figure 4b;[25,28,31]

(I) *The $Na(1)S_6$ and $Na(2)S_6$ polyhedra (edge-sharing with the $(P_{1-\delta}M_\delta)S_4$ units) as well as their "bridging" $Na(6)S_8$ quasi-cube (face-sharing with $Na(1)S_6$ and $Na(2)S_6$):* In $Na_{11+x}Sn_2P_{1-x}M_xS_{12}$, with increasing nominal x_M (equivalent to increasing $(P_{1-\delta}M_\delta)S_4$ tetrahedral volumes) $Na(1)S_6$ and $Na(6)S_8$ polyhedral volumes are increasing in both M = Sn, and Ge series (Figure 4a,c). Interestingly, the expansion of the $Na(2)S_6$ polyhedral volume is less pronounced in both series even though a direct correlation to $(P_{1-\delta}M_\delta)S_4$ tetrahedral volume is expected from the high connectivity as previously found in $Na_{11+x}Sn_{2+x}(Sb_{1-y}P_y)_{1-x}S_{12}$.[25]

(II) *The $Na(3)S_6$, $Na(4)S_6$ and $Na(5)S_6$ octahedra spanning a three-dimensionally interconnected (mostly) edge-sharing $Na(X)S_6$ network:* Besides the increasing unit cell volume with increasing nominal x_M in $Na_{11+x}Sn_2P_{1-x}M_xS_{12}$, the $Na(3)S_6$ octahedral volume is observed to be decreasing in both M = Ge, and Sn series (Figure 4a,c). The comparably small changes observed in the $Na(4)S_6$ and $Na(5)S_6$ octahedral volumes show more irregular behavior with increasing x_M in $Na_{11+x}Sn_2P_{1-x}M_xS_{12}$. Compared to $Na_{11}Sn_2PS_{12}$, in $Na_{11.625}Sn_2P_{0.375}Ge_{0.625}S_{12}$ slightly smaller and in $Na_{11.625}Sn_2P_{0.375}Sn_{0.625}S_{12}$ slightly larger $Na(4)S_6$ and $Na(5)S_6$ octahedral volumes are found. The $Na(3)S_6$, $Na(4)S_6$ and $Na(5)S_6$ octahedra have previously been observed to shrink with lattice expansion in $Na_{11+x}Sn_{2+x}(Sb_{1-y}P_y)_{1-x}S_{12}$,[25] here this effect is mainly seen in the $Na(3)S_6$ octahedral volume.

However, within $Na_{11+x}Sn_2P_{1-x}M_xS_{12}$ additional sodium has to be incorporated into the lattice further adding to the complex factors influencing the interconnected Na^+ sub-lattice. The additionally added sodium and the structural changes lead to a redistribution of sodium in the available lattice sites expressed as site occupational fractions (*sof*) shown in the Supporting Information Figure S5. Most of the observed structural parameters are comparable between

the two Ge and Sn series of $Na_{11+x}Sn_2P_{1-x}M_xS_{12}$ and the *sof* change in a similar manner as well. Overall, sodium occupancy reduces on the Na(4) and Na(5) sites, which were highly occupied in $Na_{11}Sn_2PS_{12}$, but increases on the Na(1), Na(2) and Na(3) sites that were slightly vacant in $Na_{11}Sn_2PS_{12}$. Furthermore, the Na(6) site *sof* remain low (≤ 0.08) and constant within the range of the refinement error. Accordingly, occupancies cannot be linked consistently to observed changes in Na(*X*)S_n polyhedral volumes emphasizing the complexity of the underlying Na^+ energy landscape. However, complex the sodium sublattice appears, on average its volume increases with x_M in $Na_{11+x}Sn_2P_{1-x}M_xS_{12}$ in accordance to the overall unit cell expansion (Figure S5).

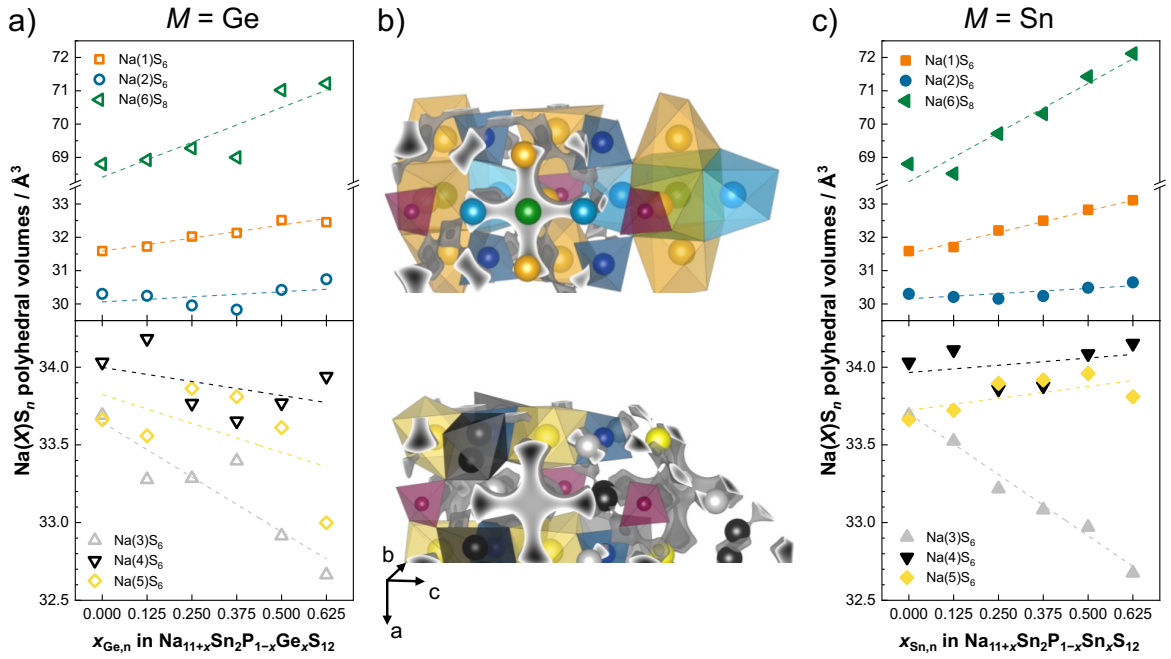

Figure 4: Volumes of the Na(X)S_n polyhedra building up the b) Na^+ diffusion pathways against the nominal a) Ge and c) Sn contents in $Na_{11+x}Sn_2P_{1-x}M_xS_{12}$. The Na(X)$S_n$ polyhedra in b) with their connectivity highlighted by the surfaces of equivalent bond valence site energies representing the energetically favored Na^+ diffusion pathways. Linear fits act as guide to the eye.

Ionic transport. In order to assess the changes of the Na^+ ionic conductivities and activation energies in $Na_{11+x}Sn_2P_{1-x}M_xS_{12}$ M = Sn, Ge, temperature-dependent electrochemical impedance spectroscopy was performed. As recently shown for this class of materials,[25,27,28,42] low-temperature measurements on sintered pellets are necessary to distinguish between in-grain and grain-boundary properties reliably.

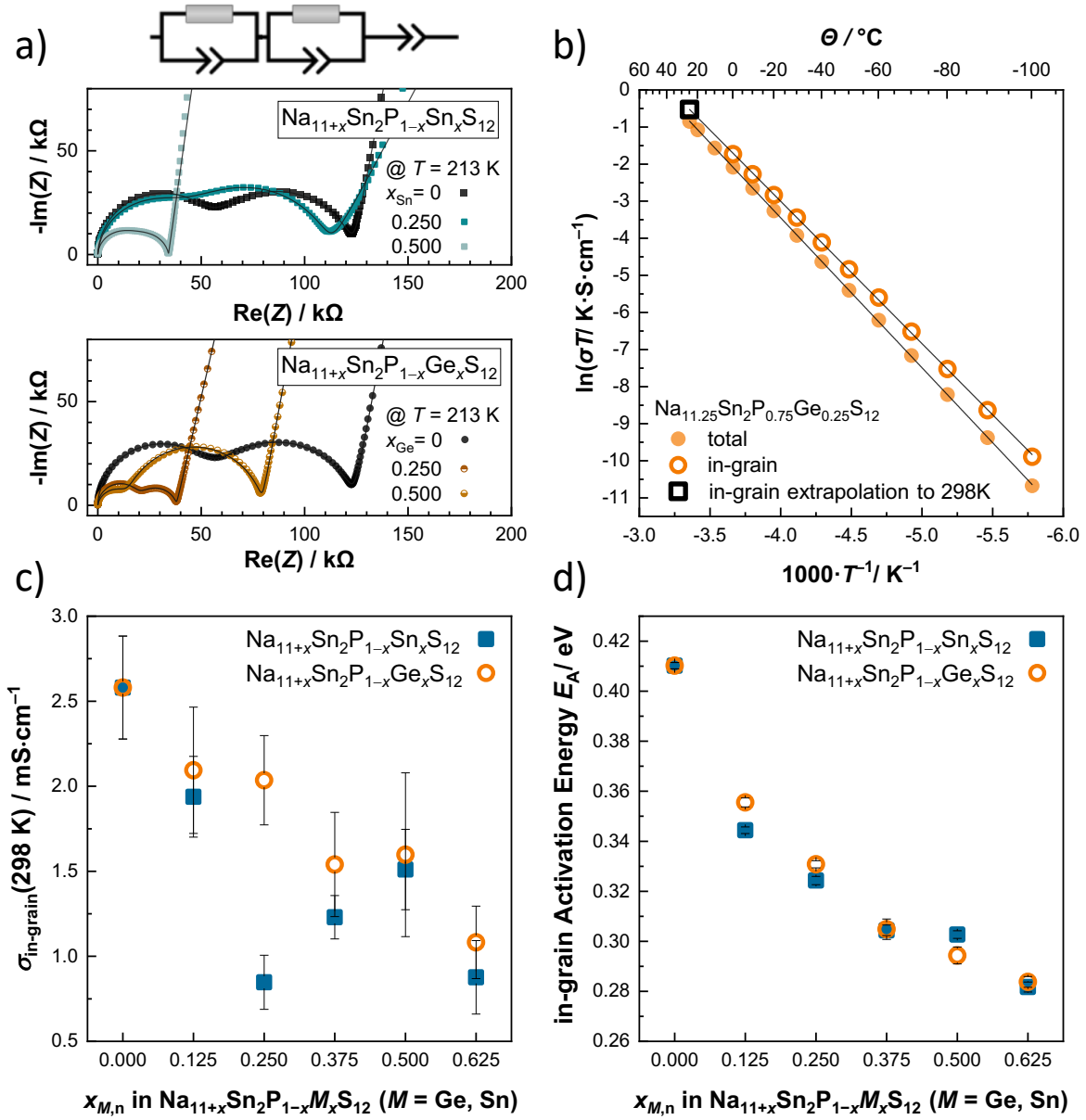

Figure 5. Nyquist representation of selected complex impedance spectra measured at 213 K (−60 °C) of $Na_{11+x}Sn_2P_{1-x}M_xS_{12}$ M = Ge, Sn with x_M = 0, 0.25, 0.5, fit (depicted as solid lines) with the displayed equivalent circuit representing contributions from in-grain and grain boundaries, respectively. b) Exemplary linearized Arrhenius representation of total and in-grain conductivities in $Na_{11.25}Sn_2P_{0.75}Ge_{0.25}S_{12}$ for determination of respective activation energies E_A and extrapolation of in-grain conductivity to 298 K. The in-grain conductivity $\sigma_{in\text{-}grain}$(298 K) in (c) as well as the in-grain activation energy E_A in (d) for $Na_{11+x}Sn_2P_{1-x}M_xS_{12}$ M = Ge, Sn is shown as a function of x_M.

In the Nyquist representation of the exemplarily shown impedance spectra, (Figure 5a) two processes can be distinguished. At lower temperatures (≤ −40 °C) the two processes are well

resolved and can be fit (as shown in Figure 5a) with equivalent circuits of two series elements consisting of a resistance in parallel with a constant phase element (CPE). The high frequency process is assigned to in-grain transport based on the capacitances of the CPE, in the range of 42 - 128 pF.[43,44] The lower frequency, depressed semicircle can be attributed to ionic transport across grain boundaries based the capacitances in the range of 0.3 - 3.1 nF.[43,44] The blocking electrode behavior expected for Au electrodes is fit with another CPE in series to the in-grain and grain-boundary processes. With higher temperatures and reduced resistances, the processes shift to higher frequencies and the in-grain process capacitive contribution and ultimately the process remains unresolved. Therefore, the in-grain Na^+ conductivities at room temperature $\sigma_{\text{in-grain}}(298\ \text{K})$ were extrapolated from the Arrhenius-like temperature dependency of conductivities as determined at lower temperatures. An exemplary linear Arrhenius fit is shown for the in-grain and the total conductivities of $Na_{11.5}Sn_2P_{0.75}Ge_{0.25}S_{12}$ in Figure 5b. From linear regression the in-grain activation energies $E_{\text{A,in-grain}}$ and respective Arrhenius pre-factors σ_0 are obtained and used to extrapolate $\sigma_{\text{in-grain}}$ to room temperature, as previously shown to be a reliable approach.[25,27,28] Errors related to $\sigma_{\text{in-grain}}(298\ \text{K})$ are obtained from error propagation of the linear regression to the Arrhenius behavior.[39] All resistances with respective Arrhenius plots and capacitances of the investigated samples in-grain and total conductivities are presented in the Supporting Information (Figure S6 and Table S14 & S15).

The resulting in-grain room-temperature ionic conductivity $\sigma_{\text{in-grain}}(298\ \text{K})$ in $Na_{11+x}Sn_2P_{1-x}M_xS_{12}$ with M = Ge, Sn is decreasing in nearly linear fashion with nominal amount of tetravalent substituent x_M (see Figure 5c). A reduction of the in-grain Na^+ conductivity of $\sigma_{\text{in-grain}}(298\ \text{K}) = 2.6\ \text{mS}\cdot\text{cm}^{-1}$ in $Na_{11}Sn_2PS_{12}$ can be observed down to $0.88\ \text{mS}\cdot\text{cm}^{-1}$ for $Na_{11.625}Sn_2P_{0.375}Sn_{0.625}S_{12}$ and to $1.1\ \text{mS}\cdot\text{cm}^{-1}$ for $Na_{11.625}Sn_2P_{0.375}Ge_{0.625}S_{12}$, respectively.

For both series of solid solutions of $Na_{11+x}Sn_2P_{1-x}M_xS_{12}$ the in-grain activation energy $E_{\text{A,in-grain}}$ (Figure 5d) is decreasing monotonically with an increasing x_M down to ~ 0.28 eV in $Na_{11.625}Sn_2P_{0.375}M_{0.625}S_{12}$ M = Ge, Sn. However, the enthalpy-entropy compensation expressed in the Meyer-Neldel rule (Figure S7) leads to the overcompensation of the reduced activation energy and therefore to the observed decrease of $\sigma_{\text{in-grain}}(298\ \text{K})$.[25,45] Overall, the total room temperature ionic conductivities (see Supporting Information Figure S8), and total activation energies, $E_{\text{A,total}}$ (in Figure S8), show similar behaviors as found for the in-grain transport properties with increasing x_M.

Structure-Transport relations. With structural parameters and transport properties monitored, certain correlations between them can be seen in the investigated series. An expanding unit cell within $Na_{11}Sn_2PS_{12}$-type materials has previously been associated with a decreasing activation energy in the anionic substitution $Na_{11.1}Sn_{2.1}P_{0.9}Se_{12}$ and cationic substitution $Na_{11+x}Sn_{2+x}(Sb_{1-y}P_y)_xS_{12}$.[25,28] Previously, it was attempted to capture this size effect by; (I) the "Na^+ channel"-volume,[32] defined as difference of unit cell volume and sum of MS_4 tetrahedral volumes following the reduction of predicted activation energies along $Na_{11}Tt_2PS_{12}$ *Tt* = Si, Ge, Sn.[32] And (II) the "average Na-S polyhedral volume",[25] defined as the average of the Na(*X*)S_n polyhedral volumes around the Na(*X*) sites *X* = 1 to 6, weighted by their multiplicities (see Equation S1). For instance, this averaged volume was used as a measure of Na^+ pathway size and is linearly correlated to the activation energy in $Na_{11+x}Sn_{2+x}(Sb_{1-y}P_y)_xS_{12}$.[25]

When trying to describe the observed reduction in the activation energy based on the average Na-S polyhedral volume as done in Figure 6a (and unit cell volume in Figure S9a), no consistent description between the series of *M* = Ge, and Sn in $Na_{11+x}Sn_2P_{1-x}Sn_xS_{12}$ can be found. Compared to literature values of $Na_{11+x}Sn_{2+x}(Sb_{1-y}P_y)_xS_{12}$ (Figure S8a), the in-grain activation energy in the $Na_{11+x}Sn_2P_{1-x}M_xS_{12}$ series is much lower despite showing a smaller expansion of the unit cell volume.[25] Overall, in contrast to literature, the average Na-S polyhedral volume does not seem to be a good descriptor for the behavior of the presently described series.

Therefore, the size effect has to be combined with the effect of additional sodium content in the structure, which can be captured here by a measure of vacancy concentration (Figure 6b). Here, this vacancy concentration $n(V_{Na})$ is estimated on a stoichiometric basis as the difference of the 13 Na(*X*) sites that are structurally available per formula unit of $Na_{11+x}Sn_2P_{1-x}M_xS_{12}$, together with the refined amount of sodium N_{Na}, normalized to the unit cell volume V_{UC} with $n(V_{Na}) = Z \cdot (13 - N_{Na})/V_{UC}$. Combining the two effects, the reduction of the in-grain activation energy seems to be reasonably described here for both *M* = Ge, Sn $Na_{11+x}Sn_2P_{1-x}M_xS_{12}$ series (Figure 6b) and seems to be consistent with previously reported literature values in $Na_{11+x}Sn_{2+x}(Sb_{1-y}P_y)_xS_{12}$ (Supporting Information Figure S9c).[25] The activation barrier increase with higher vacancy concentration may be rationalized by considering that enough Na^+ may be needed to create a flat energy landscape with Na^+ - Na^+ interactions, similar to the idea of concerted migration.[30,46]

In addition, changes in the carrier density are most likely expected to change the defect formation enthalpy. While defect formation enthalpies are often disregarded in superionic conductors, as they are thought to be negligible compared to migration enthalpy, recent reports suggest non-negligible influences of sodium or sodium vacancy concentrations in the fast ionic conductors $Na_{3-x}PS_{4-x}Cl_x$ and $Na_{3-x}M_{1-x}Zr_xCl_6$.[9,47,48] Nevertheless, while it is difficult to assess the changing defect formation enthalpies experimentally, the found trend suggests some influence of the charge carrier density on the activation barrier in $Na_{11+x}Sn_2P_{1-x}M_xS_{12}$.

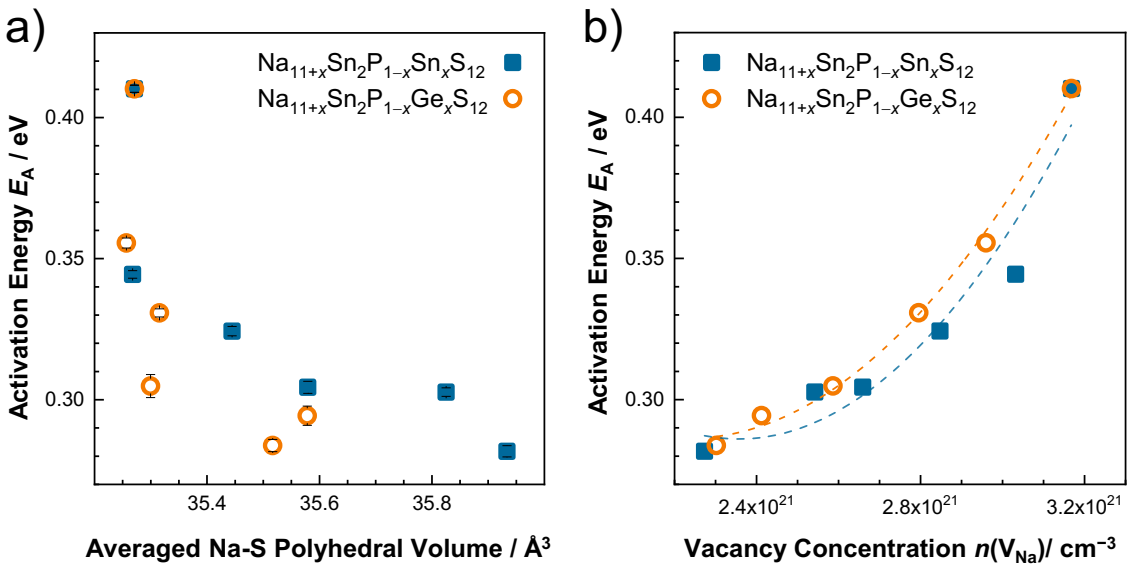

Figure 6: a) The in-grain activation energy shown against the averaged Na-S polyhedral volume showing a non-systematic decrease with larger Na^+ pathway size. b) In-grain activation energy shows an increase with stoichiometric vacancy concentration $n(V_{Na})$ in the two series of $Na_{11+x}Sn_2P_{1-x}M_xS_{12}$ M = Ge, Sn. This relation can be extended to the previously reported materials of $Na_{11+x}Sn_{2+x}(Sb_{1-y}P_y)_xS_{12}$ (see Supporting information Figure S9).[25] Parabolic fits act as guide-to-the-eye only.

5. Conclusion

Utilizing a solid-state synthesis route, the successful aliovalent substitution of P with M = Ge, Sn in $Na_{11+x}Sn_2P_{1-x}M_xS_{12}$ was achieved. The structural parameters determined by Rietveld refinement against low-temperature synchrotron X-ray diffraction show the overall lattice expansion in a linear fashion indicating the formation of solid solutions in $Na_{11+x}Sn_2P_{1-x}M_xS_{12}$ up to a solubility limit in the range of $0.5 < x_M < 0.625$. The expansion is mainly driven by the expansion of the $(P_{1-\delta}M_\delta)S_4$ tetrahedra in which germanium and tin

substitutes the phosphorous. With the expansion of the lattice and additional sodium introduced by the aliovalent substitution, changing Na(X)S_n polyhedral volumes are found leading to an overall larger Na^+ pathway. As the changes in the sodium sub-lattices in both M = Ge and Sn series of $Na_{11+x}Sn_2P_{1-x}M_xS_{12}$ are comparable, the ionic transport properties change accordingly. The room-temperature in-grain Na^+ ionic conductivity reduces with x_M down to below 1 mS·cm^{-1} as the activation energy reduces as well from 0.4 eV down to a minimum of 0.28 eV in $Na_{11.625}Sn_2P_{0.375}M_{0.625}S_{12}$. In these series of solid solutions, this reduction of the activation barrier can be best described by a reduced vacancy concentration. This work shows that aliovalent substitution can be used to alter the ionic transport properties in the $Na_{11}Sn_2PS_{12}$ structure family, by widening the explored phase width in the quasi binary $Na_4(Sn/Ge)S_4$-Na_3PS_4 system guiding future advancements and design in the $Na_{11}Sn_2PS_{12}$ structure family.

Supporting Information

The electronic Supporting Information file contains; diffraction patterns with associated Rietveld refinement, constraints applied and extracted structural information of $Na_{11+x}Sn_2P_{1-x}M_xS_{12}$ M = Ge, Sn tabulated; supporting structural parameters: site occupancy factors of Sn, P and Na(X) sites, lattice parameter ratio, $(Sn_{1-\varepsilon}M_\varepsilon)S_4$ and average Na(X)S_n volumes; obtained in-grain and total resistances with respective Arrhenius plots of $Na_{11+x}Sn_2P_{1-x}M_xS_{12}$; additional exemplary impedance spectra, Meyer-Neldel plot, total activation energies and total conductivities; in-grain activation energies in comparison to $Na_{11+x}Sn_{2+x}(Sb_{1-y}P_y)_xS_{12}$ against unit cell volume, Na concentration and vacancy concentration. The Supporting Information further contains all crystallographic information files (CIF).

AUTHOR INFORMATION

Corresponding Authors

* wzeier@uni-muenster.de

Notes

The authors declare no competing financial interests.

Acknowledgements

The research was supported by the Deutsche Forschungsgemeinschaft (DFG) under grant number ZE 1010/4-1. The authors thank Saul Lapidus for performing the synchrotron X-ray diffraction experiments at the 11-BM beamline at the Advanced Photon Source. Use of the Advanced Photon Source at Argonne National Laboratory was supported by the U. S. Department of Energy, Office of Science, Office of Basic Energy Sciences, under Contract No. DE-AC02-06CH11357.

References

(1) Janek, J.; Zeier, W. G. A Solid Future for Battery Development. *Nat. Energy* **2016**, *1* 16141.

(2) Hayashi, A.; Noi, K.; Sakuda, A.; Tatsumisago, M. Superionic Glass-Ceramic Electrolytes for Room-Temperature Rechargeable Sodium Batteries. *Nat. Commun.* **2012**, *3*, 855–856.

(3) Randau, S.; Weber, D. A.; Kötz, O.; Koerver, R.; Braun, P.; Weber, A.; Ivers-Tiffée, E.; Adermann, T.; Kulisch, J.; Zeier, W. G.; Richter, F. H.; Janek, J. Benchmarking the Performance of All-Solid-State Lithium Batteries. *Nat. Energy* **2020**, *5*, 259–270.

(4) Dewald, G. F.; Ohno, S.; Kraft, M. A.; Koerver, R.; Till, P.; Vargas-Barbosa, N. M.; Janek, J.; Zeier, W. G. Experimental Assessment of the Practical Oxidative Stability of Lithium Thiophosphate Solid Electrolytes. *Chem. Mater.* **2019**, *31*, 8328–8337.

(5) Zemann, J. Die Kristallstruktur von Lithiumphosphat, Li_3PO_4. *Acta Crystallogr.* **1960**, *13*, 863–867.

(6) Hagman, L.-O.; Kierkegaard, P.; Karvonen, P.; Virtanen, A. I.; Paasivirta, J. The Crystal Structure of $NaMe_2^{IV}(PO_4)_3$; Me^{IV} = Ge, Ti, Zr. *Acta Chem. Scand.* **1968**, *22*, 1822–1832.

(7) Guin, M.; Tietz, F. Survey of the Transport Properties of Sodium Superionic Conductor Materials for Use in Sodium Batteries. *J. Power Sources* **2015**, *273*, 1056–1064.

(8) Rossbach, A.; Tietz, F.; Grieshammer, S. Structural and Transport Properties of Lithium-Conducting NASICON Materials. *J. Power Sources* **2018**, *391*, 1–9.

(9) Schlem, R.; Banik, A.; Eckardt, M.; Zobel, M.; Zeier, W. G. $Na_{3-x}Er_{1-x}Zr_xCl_6$-A Halide-Based Fast Sodium-Ion Conductor with Vacancy-Driven Ionic Transport. *ACS Appl. Energy Mater.* **2020**, *3*, 10164–10173.

(10) Muy, S.; Voss, J.; Schlem, R.; Koerver, R.; Sedlmaier, S. J.; Maglia, F.; Lamp, P.; Zeier, W. G.; Shao-horn, Y. High-Throughput Screening of Solid-State Li-Ion Conductors Using Lattice-Dynamics Descriptors High-Throughput Screening of Solid-State Li-Ion Conductors Using Lattice-Dynamics Descriptors. *ISCIENCE* **2019**, *16*, 270–282.

(11) Steiner, H.-J.; Lutz, H. D. Neue Schnelle Ionenleiter Vom Typ $M'_3M'''C1$, (M' = Li, Na, Ag; M''' = In, Y). *Zeitschrift fur Anorg. und Allg. Chemie* **1992**, *613*, 26–30.

(12) Maekawa, H.; Matsuo, M.; Takamura, H.; Ando, M.; Noda, Y.; Karahashi, T.; Orimo, S. I. Halide-Stabilized $LiBH_4$, a Room-Temperature Lithium Fast-Ion Conductor. *J. Am. Chem. Soc.* **2009**, *131*, 894–895.

(13) Verdal, N.; Udovic, T. J.; Stavila, V.; Tang, W. S.; Rush, J. J.; Skripov, A. V. Anion Reorientations in the Superionic Conducting Phase of $Na_2B_{12}H_{12}$. *J. Phys. Chem. C* **2014**, *118*, 17483–17489.

(14) Duchene, L.; Kühnel, R.-S.; Rentsch, D.; Remhof, A.; Hagemann, H.; Battagliaa, C. A Highly Stable Sodium Solid-State Electrolyte Based on a Dodeca/Deca-Borate Equimolar Mixture. *Chem. Commun.* **2017**, *53*, 4195.

(15) Deiseroth, H.-J.; Kong, S.-T.; Eckert, H.; Vannahme, J.; Reiner, C.; Zaiß, T.; Schlosser, M. Li_6PS_5X: A Class of Crystalline Li-Rich Solids With an Unusually High Li^+ Mobility. *Angew. Chemie Int. Ed.* **2008**, *47*, 755–758.

(16) Kraft, M. A.; Ohno, S.; Zinkevich, T.; Koerver, R.; Culver, S. P.; Senyshyn, A.; Indris, S.; Morgan, B. J.; Zeier, W. G. Inducing High Ionic Conductivity in the Lithium Superionic Argyrodites $Li_{6+x}P_{1-x}Ge_xS_5I$ for All-Solid-State Batteries. *J. Am. Chem. Soc.* **2018**, *140*, 16330–16339.

(17) Minafra, N.; Kraft, M. A.; Bernges, T.; Li, C.; Schlem, R.; Morgan, B. J.; Zeier, W. G. Local Charge Inhomogeneity and Lithium Distribution in the Superionic Argyrodites Li_6PS_5X (X = Cl, Br, I). *Inorg. Chem.* **2020**, *59*, 11009–11019.

(18) Adeli, P.; Bazak, J. D.; Park, K. H.; Kochetkov, I.; Huq, A.; Goward, G. R.; Nazar, L. F. Boosting Solid-State Diffusivity and Conductivity in Lithium Superionic Argyrodites by Halide Substitution. *Angew. Chemie - Int. Ed.* **2019**, *58*, 8681–8686.

(19) Mercier, R.; Malugani, J.-P.; Fahys, B.; Robert, G.; Douglade, J. Structure Du Tetrathiophosphate de Lithium. *Acta Crystallogr. Sect. B Struct. Crystallogr. Cryst. Chem.* **1982**, *38*, 1887–1890.

(20) Kanno, R.; Murayama, M. Lithium Ionic Conductor Thio-LISICON: The Li_2S-GeS_2-P_2S_5 System. *J. Electrochem. Soc.* **2001**, *148*, A742–A746.

(21) Henseler, U.; Jansen, M. Synthesis, Structure Determination, and Ionic Conductivity Of Sodium Tetrathiophosphate. *J. Solid State Chem.* **1992**, *99*, 110–119.

(22) Kamaya, N.; Homma, K.; Yamakawa, Y.; Hirayama, M.; Kanno, R.; Yonemura, M.; Kamiyama, T.; Kato, Y.; Hama, S.; Kawamoto, K.; Mitsui, A. A Lithium Superionic Conductor. *Nat. Mater.* **2011**, *10*, 682–686.

(23) Ohno, S.; Banik, A.; Dewald, G. F.; Kraft, M. A.; Krauskopf, T.; Minafra, N.; Till, P.; Weiss, M.; Zeier, W. G. Materials Design of Ionic Conductors for Solid State Batteries. *Prog. Energy* **2020**, *2*, 022001.

(24) Zhang, Z.; Ramos, E.; Lalère, F.; Assoud, A.; Kaup, K.; Hartman, P.; Nazar, L. F. $Na_{11}Sn_2PS_{12}$: A New Solid State Sodium Superionic Conductor. *Energy Environ. Sci.* **2018**, *11*, 87–93.

(25) Kraft, M. A.; Gronych, L. M.; Famprikis, T.; Ohno, S.; Zeier, W. G. Structure and Sodium Ion Transport in $Na_{11+x}Sn_{2+x}(Sb_{1-y}P_y)_{1-x}S_{12}$. *Chem. Mater.* **2020**, *32*, 6566–6576.

(26) Jia, H.; Peng, L.; Zhang, Z.; An, T.; Xie, J. $Na_{3.8}[Sn_{0.67}Si_{0.33}]_{0.8}Sb_{0.2}S_4$: A Quinary Sodium Fast Ionic Conductor for All-Solid-State Sodium Battery. *J. Energy Chem.* **2020**, *48*, 102–106.

(27) Duchardt, M.; Ruschewitz, U.; Adams, S.; Dehnen, S.; Roling, B. Vacancy-Controlled Na^+ Superion Conduction in $Na_{11}Sn_2PS_{12}$. *Angew. Chemie Int. Ed.* **2018**, *57*, 1351–1355.

(28) Duchardt, M.; Neuberger, S.; Ruschewitz, U.; Krauskopf, T.; Zeier, W. G.; Schmedt Auf Der Günne, J.; Adams, S.; Roling, B.; Dehnen, S. The Superion Conductor $Na_{11.1}Sn_{2.1}P_{0.9}Se_{12}$: Lowering the Activation Barrier of Na^+ Conduction in Quaternary 1-4-5-6 Electrolytes. *Chem. Mater.* **2018**, *30*, 4134–4139.

(29) Heo, J. W.; Banerjee, A.; Park, K. H.; Jung, Y. S.; Hong, S. T. New Na-Ion Solid Electrolytes $Na_{4-x}Sn_{1-x}Sb_xS_4$ ($0.02 \leq x \leq 0.33$) for All-Solid-State Na-Ion Batteries. *Adv. Energy Mater.* **2018**, *8*, 1702716.

(30) Zhang, Z.; Roy, P. N.; Li, H.; Avdeev, M.; Nazar, L. F. Coupled Cation-Anion Dynamics Enhances Cation Mobility in Room-Temperature Superionic Solid-State Electrolytes. *J. Am. Chem. Soc.* **2019**, *141*, 19360–19372.

(31) Sorkin, A.; Adams, S. First-Principles Study of Superionic $Na_{9+x}Sn_xM_{3-x}S_{12}$ (M = P, Sb). *Mater. Adv.* **2020**, *1*, 184–196.

(32) Oh, K.; Chang, D.; Park, I.; Yoon, K.; Kang, K. First-Principles Investigations on Sodium Superionic Conductor $Na_{11}Sn_2PS_{12}$. *Chem. Mater.* **2019**, *31*, 6066–6075.

(33) Oh, K.; Kang, K. Planting Repulsion Centers for Faster Ionic Diffusion in Superionic Conductors. *Angew. Chemie - Int. Ed.* **2020**, *59*, 18457–18462.

(34) Jia, H.; Sun, Y.; Zhang, Z.; Peng, L.; An, T.; Xie, J. Group 14 Element Based Sodium Chalcogenide $Na_4Sn_{0.67}Si_{0.33}S_4$ as Structure Template for Exploring Sodium Superionic Conductors. *Energy Storage Mater.* **2019**, *23*, 508–513.

(35) Gao, Y.; Li, N.; Wu, Y.; Yang, W.; Bo, S. Rethinking the Design of Ionic Conductors Using Meyer – Neldel – Conductivity Plot. *Adv. Energy Mat.* **2021**, *11*, 2100325.

(36) Coelho, A. A. TOPAS-Academic. Brisbane, Australia 2007.

(37) Chen, H.; Wong, L. L.; Adams, S. SoftBV – a Software Tool for Screening the Materials Genome of Inorganic Fast Ion Conductors. *Acta Crystallogr. Sect. B Struct. Sci. Cryst. Eng. Mater.* **2019**, *75*, 18–33.

(38) Momma, K.; Izumi, F. VESTA: A Three-Dimensional Visualization System for Electronic and Structural Analysis. *J. Appl. Crystallogr.* **2008**, *41*, 653–658.

(39) Ohno, S.; Bernges, T.; Buchheim, J.; Duchardt, M.; Hatz, A. K.; Kraft, M. A.; Kwak, H.; Santhosha, A. L.; Liu, Z.; Minafra, N.; Tsuji, F.; Sakuda, A.; Schlem, R.; Xiong, S.; Zhang, Z.; Adelhelm, P.; Chen, H.; Hayashi, A.; Jung, Y. S.; Lotsch, B. V.; Roling, B.; Vargas-Barbosa, N. M.; Zeier, W. G. How Certain Are the Reported Ionic Conductivities of Thiophosphate-Based Solid Electrolytes? An Interlaboratory Study. *ACS Energy Letters*. **2020**, *5*, 910–915.

(40) Richards, W. D.; Tsujimura, T.; Miara, L. J.; Wang, Y.; Kim, J. C.; Ong, S. P.; Uechi, I.; Suzuki, N.; Ceder, G. Design and Synthesis of the Superionic Conductor

$Na_{10}SnP_2S_{12}$. *Nat. Commun.* **2016**, *7*, 11009.

(41) Shannon, R. D. Revised Effective Ionic Radii and Systematic Studies of Interatomic Distances in Halides and Chalcogenides. *Acta Crystallogr. Sect. A* **1976**, *32*, 751–767.

(42) Yu, Z.; Shang, S.-L.; Wang, D.; Li, Y. C.; Yennawar, H. P.; Li, G.; Huang, H.-T.; Gao, Y.; Mallouk, T. E.; Liu, Z.-K.; Wang, D. Synthesis and Understanding of $Na_{11}Sn_2PSe_{12}$ with Enhanced Ionic Conductivity for All-Solid-State Na-Ion Battery. *Energy Storage Mater.* **2019**, *17*, 70–77.

(43) Brug, G. J.; van den Eeden, A. L. G.; Sluyters-Rehbach, M.; Sluyters, J. H. The Analysis of Electrode Impedances Complicated by the Presence of a Constant Phase Element. *J. Electroanal. Chem.* **1984**, *176*, 275–295.

(44) Irvine, J. T. S.; Sinclair, D. C.; West, A. R. Electroceramics: Characterization by Impedance Spectroscopy. *Advanced Materials*. **1990**, *2*,132–138.

(45) Muy, S.; Bachmann, J. C.; Giordano, L.; Chang, H.-H.; Abernathy, D. L.; Bansal, D.; Delaire, O.; Hori, S.; Kanno, R.; Maglia, F.; Lupart, S.; Lamp, P.; Zeier, W. G.; Shao-Horn, Y. The Role of Lattice Dynamics on the Lithium Conductivity of Li_3PO_4-Li_3VO_4-Li_4GeO_4 Lithium Superionic Conductors. *Energy Environ. Sci.,* **2018***, 11,* 850–859.

(46) He, X.; Zhu, Y.; Mo, Y. Origin of Fast Ion Diffusion in Super-Ionic Conductors. *Nat. Commun.* **2017**, *8*, 15893.

(47) Chu, I. H.; Kompella, C. S.; Nguyen, H.; Zhu, Z.; Hy, S.; Deng, Z.; Meng, Y. S.; Ong, S. P. Room-Temperature All-Solid-State Rechargeable Sodium-Ion Batteries with a Cl-Doped Na_3PS_4Superionic Conductor. *Sci. Rep.* **2016**, *6*, 33733.

(48) Wu, E. A.; Banerjee, S.; Tang, H.; Richardson, P. M.; Doux, J. M.; Qi, J.; Zhu, Z.; Grenier, A.; Li, Y.; Zhao, E.; Deysher, G.; Sebti, E.; Nguyen, H.; Stephens, R.; Verbist, G.; Chapman, K. W.; Clément, R. J.; Banerjee, A.; Meng, Y. S.; Ong, S. P. A Stable Cathode-Solid Electrolyte Composite for High-Voltage, Long-Cycle-Life Solid-State Sodium-Ion Batteries. *Nat. Commun.* **2021**, *12*, 1256.

Table of contents entry